scientific reports

Check for updates

OPEN

# Novel metal–organic framework biosensing platform for detection of COVID-19 RNA

Aya Elgazar[1], Rana Sabouni[1]✉, Mehdi Ghommem[2] & Amin F. Majdalawieh[3]

**The latest pandemic resulting from the novel SARS-CoV-2 coronavirus has significantly affected public health, the worldwide economy, and social life. Metal organic frameworks (MOFs) are currently being implemented in biosensors for rapid and accurate detection of viruses thanks to their exceptional properties. This research aims to develop a Zeolitic Imidazolate Framework-8 (ZIF-8) based fluorescent biosensor for facile and rapid COVID-19 RNA sequence detection. ZIF-8 was characterized using several tests, such as FT-IR, TGA, and PXRD, to examine the MOF's crystalline structure and thermal stability. The results demonstrated high crystallinity and thermal stability up to a temperature of 550 °C. The experimental study showed that ZIF-8 is an excellent fluorescence quencher, with 78.39% quenching efficiency. Analyzing the adsorption mechanism of probe DNA into ZIF-8 revealed that they can form electrostatic and π–π stacking interactions, forming a P-DNA@ZIF-8 complex and that PET is more dominant than FRET in the quenching mechanism. This ZIF-8 biosensing platform showed high sensitivity towards COVID-19 RNA with an ultra-low limit of detection of 6.24 pM, a rapid detection time of 8 min, and high selectivity to COVID-19 RNA. Indeed, ZIF-8 experienced much lower fluorescence recovery when tested on two mismatched RNAs. The experimental results show the potential use of ZIF-8 as a novel biosensor for a rapid and sensitive COVID-19 diagnosis.**

**Keywords** ZIF-8, Metal–organic frameworks, Biosensor, COVID-19 RNA sequence, Probe DNA, Detection limit

**List of symbols**

| | |
|---|---|
| COVID-19 | Coronavirus disease 2019 |
| RT-PCR | Reverse transcription polymerase chain reaction |
| MOF | Metal organic framework |
| ZIF-8 | Zeolitic Imidazolate Framework-8 |
| SPR | Surface plasmon resonance |
| ELISA | Enzyme-linked immunosorbent assay |
| P-DNA | Probe DNA |
| T-RNA | Target RNA |
| PXRD | Powder X-ray diffraction |
| FT-IR | Fourier transform infrared |
| FE-SEM | Field emission scanning electron microscopes |
| TGA | Thermogravimetric analysis |
| BET | Brunauer–Emmett–Teller |
| $Q_e$ | Quenching efficiency |
| LOD | Limit of detection |
| $K_b$ | Binding constant |
| n | Number of binding sites |
| FRET | Fluorescence resonance energy transfer |
| PET | Photoinduced electron transfer |
| $K_{sv}$ | Stern–Volmer constant |
| $K_q$ | Quenching rate |
| $\tau_0$ | Lifetime decay |

[1]Department of Chemical and Biological Engineering, American University of Sharjah, 26666, Sharjah, United Arab Emirates. [2]Department of Mechanical Engineering, American University of Sharjah, 26666, Sharjah, United Arab Emirates. [3]Department of Biology, Chemistry, and Environmental Sciences, College of Arts and Sciences, American University of Sharjah, 26666, Sharjah, United Arab Emirates. ✉email: rsabouni@aus.edu

As reported by the World Health Organization (WHO), as of 9:06 pm GST, 21 March 2023, there have been 761,071,826 confirmed cases of Coronavirus disease 2019 (COVID-19) worldwide, of which 6,879,677 were death cases[1]. The disease's alarming spread has led governments to implement stringent measures across the world to control and stop the virus from spreading. These measures included full lockdowns, suspension of flights, border closures, and public respiratory hygiene measures[2,3]. Even though the virus is currently relatively under control because of the mass vaccination campaigns, it still presents a threat to public health, global economies, and societal standards.

One of the most crucial factors in controlling the spread of the virus is an early, fast, and precise diagnosis. Currently, the two main COVID-19 diagnostic techniques are antibody detection kits and Real-Time Reverse Transcription Polymerase Chain Reaction (RT-PCR)[4,5]. Although the latter test has relatively high accuracy, it is time-demanding and needs costly equipment and skillful personnel to operate the procedure[6,7]. Moreover, the risk of cross-contamination and non-specific amplification can result in inaccurate results[8]. Antibody detection kits are comparatively less accurate and detect the viral infection after the virus triggers the immune system[9]. Therefore, there is still a need for more efficient and accessible diagnostic methods for the COVID-19 virus.

Metal organic frameworks (MOFs) are a new material type that exhibits very high porosity and crystallinity. MOFs mainly consist of metal ions that are linked via organic linkers. The properties of MOFs, such as high porosity, large surface area, and controllable pore size, render them excellent candidates for different applications, including molecular diagnosis and biosensing[10–12]. MOFs have also been used as fluorescent sensors for detecting different small biomolecules, including viruses[13]. One MOF that has gained significant attention in biosensing applications is Zeolitic Imidazolate Framework-8 (ZIF-8). ZIF-8 MOF exhibits a unique structure comprising zinc ions and imidazole ligands. It also exhibits many unique properties that render it a distinctive choice for the development of a COVID-19 RNA biosensor. For instance, ZIF-8 has a microstructure that typically falls within the nanometer range, with crystals often ranging from 50 to 200 nm, offering a large surface area[14,15]. This large surface area allows for the immobilization of a significant number of probe DNA molecules, enhancing the sensitivity of the biosensor. Moreover, the high stability of ZIF-8 in different environments over time ensures a reliable and long-term performance of the biosensor. ZIF-8 is also known for its low toxicity, and its biocompatibility is one of the reasons it is widely used in various biomedical and environmental applications[16]. Overall, ZIF-8's combination of high surface area, tunable pore size, stability, biocompatibility, and ease of functionalization sets it apart from other materials commonly used in biosensor development such as gold nanoparticles and graphene oxide[17–19].

Moreover, ZIF-8 is an excellent fluorescence quencher, making it an ideal candidate for optical biosensing. Pan et al. used a ZIF-8 fluorescent biosensor for detecting HIV ss-DNA with an LOD of 1.2 nM[20]. In addition, another study prepared an N-doped carbon using ZIF-8 as a precursor to detect Zika virus RNA sequences. This sensing platform exhibited high chemical stability and good conductivity and was inexpensive[21]. Limited research findings exist concerning the use of MOFs as sensing platforms for COVID-19. Indeed, previous studies mainly focused on the detection of COVID-19 spike protein through electrochemical[22–24], colorimetric[25], optical[26,27], SPR[28], and ELISA[29] assays. Yet, there has been limited exploration into applying MOFs as fluorescent-based sensing platforms for COVID-19 nucleic acid detection, specifically COVID-19 RNA sequences. In the literature, there is only a single, preliminary investigation conducted by Alkodairy et al on the use of ZIF-8 for the detection of COVID-19 RNA, with no detailed elucidation of the associated attachment mechanism[30]. Therefore, there is a significant gap in the existing literature and a shortage of studies in this specific area. The present study utilizes ZIF-8 as a novel fluorescent biosensing platform for rapidly and accurately sensing COVID-19 RNA sequences. Our paper comprehensively examines and investigates this biosensing platform's sensitivity, selectivity, and recyclability. Several factors were optimized to understand and explain the detection mechanism including incubation time and MOF dosages. Detailed characterization tests such as XRD, FTIR, BET, and TGA were conducted to support the effectiveness of ZIF-8 in the detection of COVID-19 RNA. The study also investigates the quenching and detection mechanisms of the biosensor through conducting several experiments including time decay and UV–Vis absorption spectrum analysis. Furthermore, the study estimates crucial parameters such as the binding constant ($K_b$) and the Stern–Volmer constant ($K_{sv}$). The work revealed the high sensitivity, low limit of detection, and elevated selectivity of ZIF-8 to COVID-19 RNA sequences in vitro, making it a potential detector material for biosensors.

The remainder of the paper is organized into three main sections. Section "Experimental methodology" presents the materials and apparatus used in the study, and detailed experimental methodology. Section "Results and discussion" discusses the results obtained from the experiments related to the characterization, sensitivity, and selectivity of the proposed biosensing platform. Finally, the conclusion summarizes the present study's key findings and offers suggestions for future research.

## Experimental methodology

Figure 1 depicts a schematic diagram that illustrates the detection mechanism of the proposed ZIF-8-based biosensor. ZIF-8 is combined with FAM single-stranded probe DNA (P-DNA) via electrostatic or π–π stacking interactions, producing a P-DNA@MOF sensing platform. These interactions induce the quenching of the P-DNA fluorescence. When the complementary target RNA (T-RNA) is introduced into the system, the P-DNA interacts with the target RNA to form a hybrid duplex. This duplex is very stable and causes the P-DNA to be desorbed from ZIF-8, resulting in fluorescence recovery.

### Materials and apparatus

Commercial ZIF-8, zinc nitrate hexahydrate, and 2-methylimidazole were bought from Sigma-Aldrich and used without additional purification. ZIF-8 was purchased under the trademark Basolite® Z1200. The sequence of

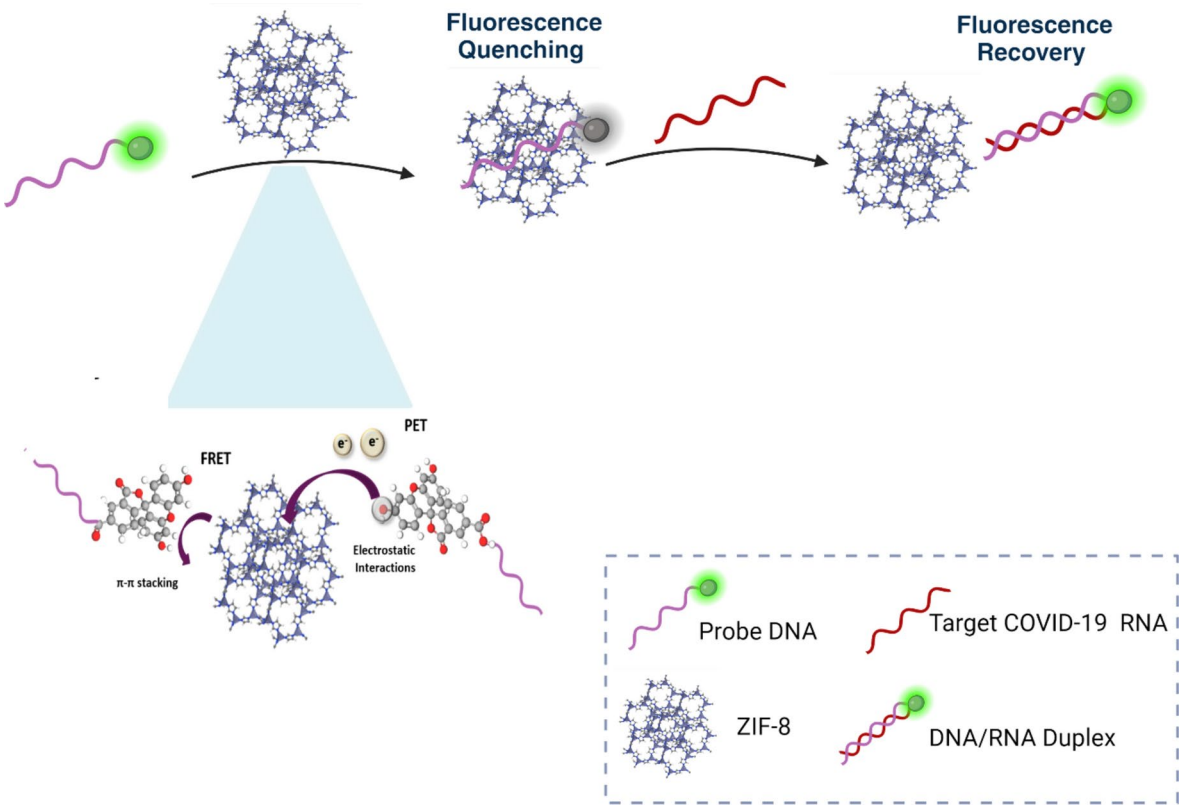


**Fig. 1**. Detection Mechanism of ZIF-8-based Fluorescent Biosensor for the Target COVID-19 RNA.

the P-DNA is 5′-FAM-AGATGTCTTGTGCTGCCGGTA-3′, and the sequences of the T-RNA, single-base pair mutated RNA (T1), and two-base pair mutated RNA (T2) are UACCGGCAGCACAAGACAUCU, UACCGGCAGCAC**C**AGACAUCU, and UACCGGCAGCAC**C**AGAC**G**UCU, respectively. All the DNA and RNA sequences were obtained from GenScript (New Jersey, United States). All the RNA and DNA samples were prepared to a concentration of 100 μM in TE buffer solution (10 mM Tris pH 8.0, 0.1 mM EDTA) and stored at -20 °C (DNA) and − 80 °C (RNA) for use.

Fluorescence measurements were conducted using a DW-F97Pro fluorescence spectrometer from Drawell, China. The spectrometer's excitation source is a 150W xenon lamp (Hamamatsu) with an emission and excitation wavelength range of 200–900 nm. The spectrometer is also accompanied by the software NoelG_F, which is used to record and process the measurements of the fluorescence spectrometer. The absorption spectra were measured using a UV–Vis spectrophotometer (Evolution 60 s, USA; resolution > 1.5 at 1.0 nm spectral bandwidth). The lifetime decay measurements were obtained using a QuantaMaster Phosphorescence Spectrofluorometer (Photon Technology International, Edison, NJ, USA). The crystal structure of ZIF-8 was verified by processing Powder X-ray diffraction (PXRD) measurements on a Bruker D8 ADVANCE system, and they were collected over a 2θ range of 5.0–60°. Field Emission Scanning Electron Microscope (FE-SEM) was conducted to examine the MOF's shape and crystallite morphology. FE-SEM was run at the University of Western Ontario, Canada, using Hitachi SU8230 Regulus Ultra High-Resolution Field Emission SEM. Fourier transform infrared (FT–IR) spectra were acquired using the FT–IR spectrophotometer (PerkinElmer, USA) after diluting the sample with transmission KBr and using the pressed-disc technique. The spectrophotometer operated in a range of 4000–450 $cm^{-1}$, had a resolution of 1.0 $cm^{-1}$, and ten scans were signal-averaged. Thermogravimetric analysis (TGA) of ZIF-8 was conducted using Pyris-1 TGA instrument (PerkinElmer, USA), with a 20 °C $min^{-1}$ heating rate and a temperature range of 25–800 °C using nitrogen and helium as inert gases. The MOF's specific surface area was measured using the Autosorb-iQ instrument. The ASiQwin™ software used for the analysis calculated the specific surface area using the multipoint BET method.

## COVID-19 RNA detection experiments

*P-DNA quenching experiment*

The detection of COVID-19 RNA sequences was assessed by measuring the P-DNA fluorescence by fluorescence spectrometry while operating at room temperature. For the quantitative analysis, the fluorescence emission wavelength was 518 nm with excitation at 490 nm. First, an experiment to find ZIF-8's quenching efficiency toward the fluorescence of P-DNA was conducted by sequentially adding 75 μL of ZIF-8 solution (0.7 mg/ml) to a solution of P-DNA (10 nM) in TE buffer forming a P-DNA@MOF complex. The corresponding fluorescence spectrum for each concentration was measured until reaching saturation. The quenching efficiency ($\%Q_e$) was computed as per Eq. (1):

$$\%Q_e = \frac{F_0 - F_M}{F_0} * 100\% \quad (1)$$

where $F_0$ is the P-DNA fluorescence intensity without ZIF-8 and $F_M$ is the P-DNA fluorescence intensity with ZIF-8 measured at 518 nm wavelength.

*Limit of detection (LOD)/target RNA recovery*

The fluorescence recovery experiment was carried out at ambient conditions (about 23 °C) by sequentially adding 50 µL of target RNA (200 pM) to the above P-DNA@ZIF-8 complex. The corresponding spectrum for each concentration was measured until no further recovery in fluorescence was noticed. The efficiency of fluorescence recovery was estimated following Eq. (2)

$$RE = \frac{F_T}{F_M} - 1 \quad (2)$$

where $F_T$ is the fluorescence intensity of the solution in the presence of T-RNA, and $F_M$ is the fluorescence intensity of the solution in the absence of T-RNA, respectively.

The limit of detection (LOD) is the lowest concentration of COVID-19 RNA sequences that can be reliably detected with the sensing platform. The previous procedure was repeated twice to find the LOD, and a regression for fluorescence against T-RNA concentration was generated. The linear section of the regression was used to calculate the LOD using the following formula:

$$LOD = \frac{3\sigma}{m} \quad (3)$$

where σ is the standard deviation, and m is the slope of the linear fitting of the curve showing fluorescence as a function of the T-RNA concentration.

## Results and discussion

### Characterization of the detector material ZIF-8

The detector material ZIF-8 was characterized by conducting XRD, FT-IR, FE-SEM, TGA, and $N_2$ adsorption tests. The associated results are displayed in Fig. 2. The chemical stability of ZIF-8 was tested in different chemical environments over three days, including open air, ethanol, HCl (1 M), NaOH (1 M), and acetone. Subsequently,

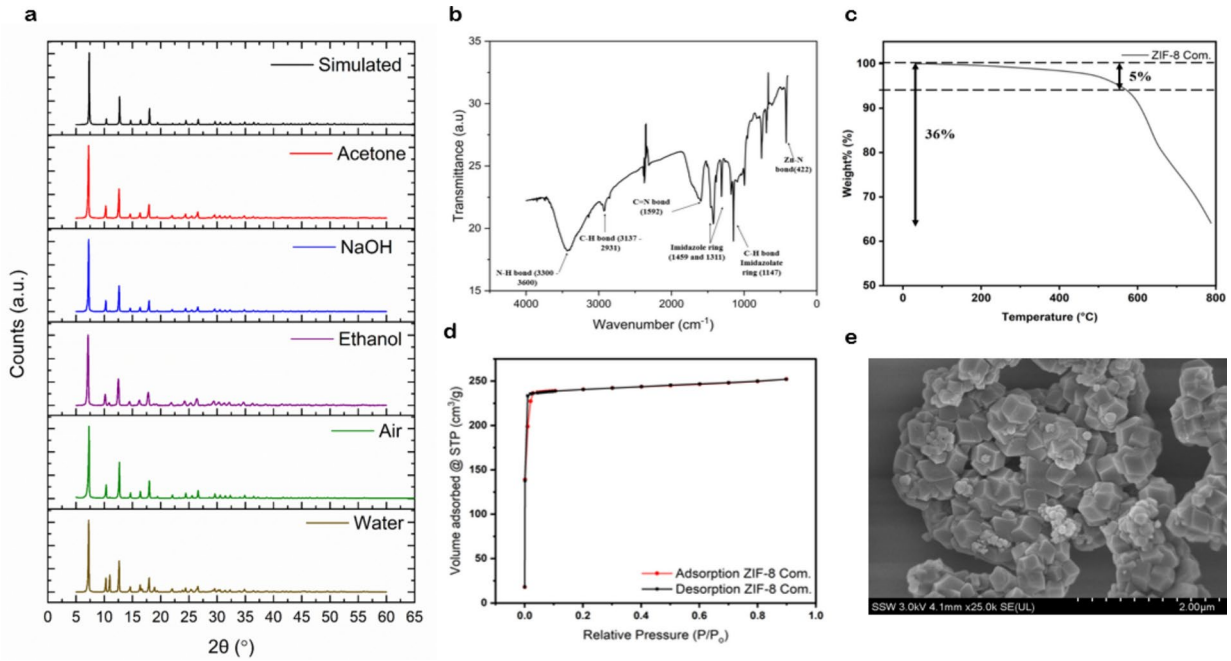


**Fig. 2**. (**a**) Simulated PXRD and measured PXRD of ZIF-8 in different chemical environments. (**b**). FT-IR spectrum of ZIF-8. (**c**) TGA results of ZIF-8. (**d**) BET isotherm of ZIF-8. (**e**) FE-SEM of ZIF-8.

PXRD analysis was performed. Figure 2a represents the simulated PXRD of ZIF-8 along with the measured PXRD patterns in different environments. ZIF-8 exhibited major diffraction peaks at $2\theta = 7.45°$, 10.5°, 12.8°, 14.8°, 16.5°, and 18.1°, with the sharpest peak at $2\theta = 7.45°$. These peaks are associated with planes (110), (200), (211), (220), (310), and (222), respectively, which reflect the significant crystallinity of ZIF-8. Figure 2a shows that all the samples' peaks possess unaltered positions and retain their original crystalline structure, indicating the high stability of ZIF-8 in these different environments. However, the ZIF-8 sample dissolved in water showed a new peak at position $2\theta \cong 11$, which is not a characteristic peak of ZIF-8. This peak can be attributed to the presence of a new phase of crystallites, which caused a slight structural instability[31]. On the other hand, the ZIF-8 sample dissolved in HCl reacted completely with the solvent and was re-crystalized into a salt complex, indicating the low chemical stability of ZIF-8 in acidic mediums[32]. Therefore, an XRD could not be obtained for the ZIF-8 sample in the HCl medium. The obtained patterns of the MOF closely resembled those reported in previous research studies on lab-synthesized ZIF-8s[33,34].

The FTIR spectrum of ZIF-8, shown in Fig. 2b, is consistent with the literature[20,35]. The N–H bond stretching is confirmed by the broad peak in the range 3300–3600 $cm^{-1}$, while the minor peaks at 3137 $cm^{-1}$ and 2931 $cm^{-1}$ correspond to the stretching of aromatic and aliphatic C–H of the methyl group and imidazole ring in the organic linker, respectively[35]. Moreover, the peak at 1592 $cm^{-1}$ presents the vibration of the C=N stretch mode. The whole imidazole ring vibration caused firm peaks at 1459 $cm^{-1}$ and 1311 $cm^{-1}$[35]. In addition, the peak at 1147 $cm^{-1}$ is linked to the C–H bending in the imidazolate[36]. The spectral bands in the 1000–900 $cm^{-1}$ range are assigned to bending the ring's in-plane, while the peaks at 760 $cm^{-1}$ and 694 $cm^{-1}$ are for the out-of-plane binding[20]. Finally, the intense band observed at 422 $cm^{-1}$ is ascribed to the Zn–N stretching. The TGA method was used to test the stability of ZIF-8, and the results are shown in Fig. 2c. The results indicate that the obtained thermal stability of ZIF-8 was consistent with that reported in the literature[20]. As seen in Fig. 2c, the overall weight loss of the sample was about 36%. Moreover, there was a gradual decrease in the weight of 5% at the beginning, corresponding to the loss of moisture and any trapped solvent molecules in the MOF. The TGA traces also revealed a significant weight decrease after 550 °C. Hence, it can be concluded that ZIF-8 has good thermal stability when operating below the temperature of 550 °C, which implies the high stability of the biosensor given the expected operating temperature. Figure 2d displays the $N_2$ adsorption/desorption isotherm of ZIF-8 nanocrystals using BET theory. BET theory describes the physical adsorption of gas particles on the solid's surface, and it serves as the basis for this analysis method, which can provide the specific surface area of MOFs[37]. The isotherm of ZIF-8 exhibits a typical type I isotherm, which compares well with reported isotherms in literature[38]. Type I isotherm indicates that ZIF-8 has a microporous structure. The surface area (pore volume) of ZIF-8 was obtained as 1032 $m^2/g$ (0.343 $cm^3/g$). The fast uptake observed in the area of low pressure is a feature of adsorption in micropores. The BET results revealed a high surface area for ZIF-8, which provides more active sites for the binding of T-RNA and P-DNA, thus increasing the sensitivity of the biosensor and lowering its limit of detection. FE-SEM is a technique used to generate a microstructure image of MOFs. Figure 2e shows the FE-SEM of ZIF-8. The FE-SEM micrograph shows the rhombic polyhedral morphologies of ZIF-8. Also, the particle size of ZIF-8 was calculated from the FE-SEM graph using ImageJ software and was determined to be ~ 237 nm, which compares well with the results reported in the literature[39]. The consistent particle size observed would ensure uniform diffusion rates and consistent interaction with the P-DNA, reducing variability and improving the reproducibility of the response of the biosensor.

## Detection of COVID-19 RNA sequence

*Quenching ability of ZIF-8 towards P-DNA*

ZIF-8 is considered to have strong fluorescence quenching properties and can quench the FAM dye attached to the P-DNA. To test this property, a solution of ZIF-8 was sequentially added to the P-DNA, and the resulting fluorescence was recorded. The addition of the MOF reduced the P-DNA fluorescence intensity, as seen in Fig. 3a, indicating that ZIF-8 can effectively quench the P-DNA fluorescence. Inspecting Fig. 3a, we observe that the P-DNA fluorescence intensity gradually decreases up to the saturation concentration of ZIF-8, which was found to be 217.2 µg/ml. The ZIF-8 quenching efficiency ($\%Q_e$) was calculated to be 78.32% with a standard deviation of 0.1949% and a confidence interval of 78.013–78.633% from four fluorescence measurement trials. The high quenching efficiency can be attributed to the large surface area of ZIF-8 which provides more binding sites for the attachment of P-DNA, leading to the enhancement of the interactions between the P-DNA and ZIF-8. Also, the metal nodes and the organic linkers within ZIF-8 facilitate efficient energy transfer from the P-DNA.

The binding ability of ZIF-8 to the P-DNA was determined by calculating the apparent binding constant ($K_b$) using the double logarithm, given by Eq. (4):

$$\frac{\log(F_0 - F)}{F} = n\log\,[C_{ZIF-8}] + \log K_b \tag{4}$$

where $F_0$ and F are the fluorescence intensities of P-DNA at 518 nm with and without ZIF-8, $C_{ZIF-8}$ is the concentration of ZIF-8 in molar at each fluorescence intensity, $K_b$ is the binding constant, and (n) is the number of binding sites[40]. The $K_b$ and (n) values were equal to $1.186 \times 10^5\ M^{-1}$ and 1.56, respectively. $K_b$ and (n) of ZIF-8 toward the P-DNA further explain the high quenching efficiency of ZIF-8. Figure 3b represents the impact of incubation time with ZIF-8 on the P-DNA emission spectra. The fluorescence intensity decreased with further incubation with ZIF-8 and remained approximately unchanged after 30 min. Therefore, 30 min was selected as the optimum incubation time for the P-DNA and ZIF-8.

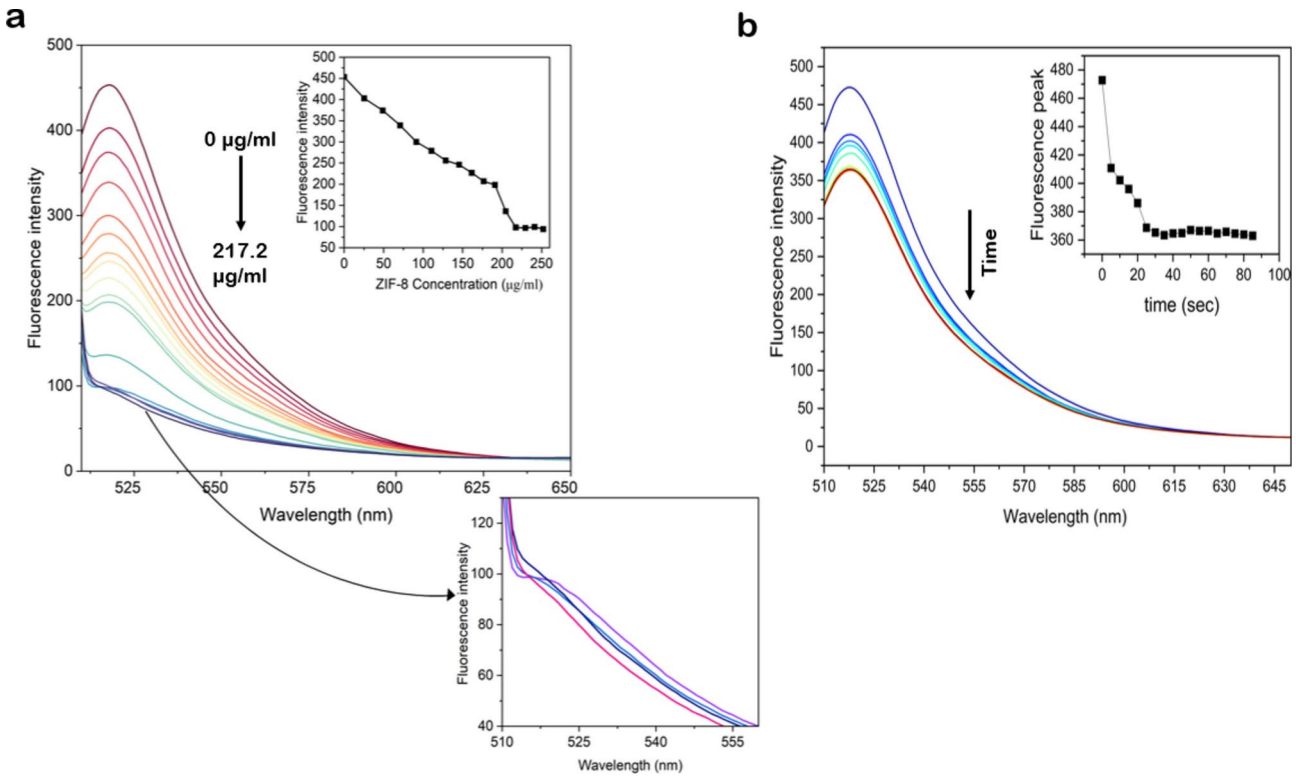


**Fig. 3**. The P-DNA fluorescence emission spectra. (**a**) P-DNA fluorescence spectrum (10 nM) incubated with varying concentrations of ZIF-8 in TE buffer with an incubation time of 30 min. (**b**) P-DNA fluorescence spectrum of (10 nM) with varying incubation time with ZIF-8 in TE buffer.

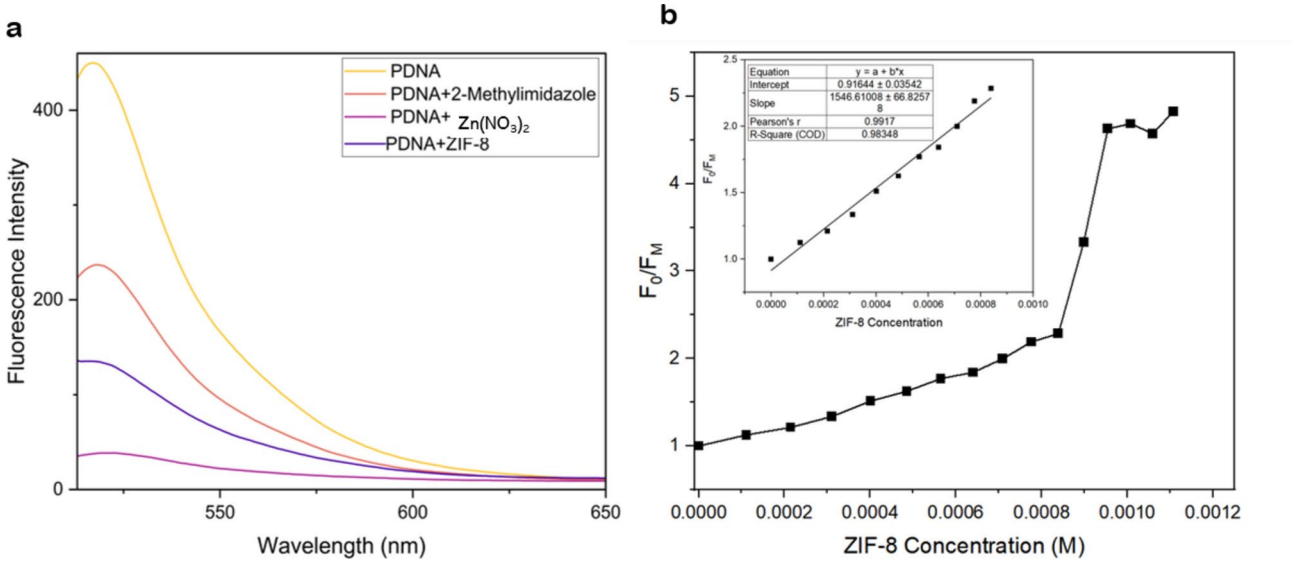


**Fig. 4**. (**a**) The P-DNA fluorescence emission spectra (10 nM) in ZIF-8, 2-methylimidazole, and $Zn(NO_3)_2$ in TE buffer. (**b**) The Stern–Volmer (S–V) relation for the fluorescence quenching of P-DNA by ZIF-8 (0–0.00111 M).

*Mechanism of P-DNA adsorption on ZIF-8*

The negatively charged aromatic P-DNA is adsorbed on ZIF-8 through three interactions, which are hydrogen bonding, electrostatic interactions, and π–π stacking interactions. Therefore, to further understand the quenching features and mechanism of ZIF-8, the P-DNA fluorescence quenching efficiencies of ZIF-8 precursors, 2-methylimidazole and zinc hexahydrate nitrate, were measured. The results presented in Fig. 4a

indicate that 2-methylimidazole could partially quench the fluorescence of the P-DNA, with $\%Q_e$ of 48.5% with a standard deviation of 1.90% based on two trials. This effect can be explained by the π-electron stacking system in the imidazolate ring. The aromatic rings of the nucleotide bases in the probe DNA align with the aromatic rings or π systems present in ZIF-8, providing an additional layer of stabilization. This stabilization forms a network of attractive forces that enhances the overall structural integrity of the P-DNA@ZIF-8 complex. Hence, the 2-methylimidazole linker can adsorb P-DNA and quench it by fluorescence resonance energy transfer (FRET). Moreover, it was observed that $Zn(NO_3)_2$ completely quenched the P-DNA fluorescence, with a $\%Q_e$ of 91.28% with a standard deviation of 0.311% based on two trials. This significant decrease in fluorescence can be ascribed to the inherent quenching ability of $Zn^{2+}$ ions. The electrostatic binding of zinc ions with the phosphate backbones in the P-DNA and their intercalations into the base pairs of the probe DNA trigger a photoinduced electron transfer (PET) process from the dye attached to the P-DNA (FAM) to the zinc ions, quenching its fluorescence[41,42]. Consequently, it can be deduced that the P-DNA is adsorbed into ZIF-8 by mainly electrostatic and π–π stacking interactions, producing a P-DNA@ZIF-8 complex.

Several other studies were conducted to support the above claim further. The quenching mechanism of P-DNA can be further explained through the Stern–Volmer equation:

$$\frac{F_o}{F_M} = 1 + K_{sv}\,[C_{ZIF-8}] \;\text{ while }\; K_{sv} = K_q \tau_0 \tag{5}$$

where $F_0$ and $F_M$ are the fluorescence intensity of P-DNA before and after the addition of ZIF-8, $K_{sv}$ is the Stern–Volmer constant, $[C_{ZIF\text{-}8}]$ is the molar concentration of ZIF-8, $K_q$ represents the quenching constant and $\tau_0$ denotes the lifetime of the P-DNA without the addition of ZIF-8[43]. The correlation between $F_0/F_M$ and $[C_{ZIF\text{-}8}]$ follows a linear pattern, suggesting a dynamic quenching mechanism. Any deviation from linearity indicates that the quenching can be either static or a simultaneous combination of static and dynamic quenching. In static quenching, a complex structure forms between the quencher and the fluorescent probe in the ground state. However, during the dynamic quenching, the electron transfer takes place between the quencher and the fluorescent probe in the excited state[44].

As shown in Fig. 4b, the S–V graph exhibits a linear behavior for most of the ZIF-8 concentration range, suggesting dynamic quenching. The $K_{sv}$ value was found from the plot to be 1546.6 $M^{-1}$. This relatively large $K_{sv}$ value indicates higher sensitivity and more interactions among the P-DNA and ZIF-8. To further validate the quenching mechanism, the P-DNA fluorescence decay was examined with and without ZIF-8 at 518 nm with an excitation wavelength of 490 nm (Fig. 5a). The calculated lifetime decay of the P-DNA was 10.76 µs. Moreover, the lifetime decay of P-DNA after adding ZIF-8 remained almost unchanged (10.40 µs), confirming a typical dynamic quenching process for P-DNA. Finally, the $K_q$ value was calculated as $1.437 \times 10^8$. A high $K_q$ value ensures a faster quenching rate for ZIF-8. On the other hand, observing Fig. 5b, the UV–Vis absorption spectrum of ZIF-8 does not overlap with the emission spectrum P-DNA, indicating a low contribution of fluorescence resonance energy transfer (FRET) towards the quenching of the P-DNA. Therefore, the above investigations confirm the dominance of the photoinduced electron transfer (PET) process in the quenching mechanism.

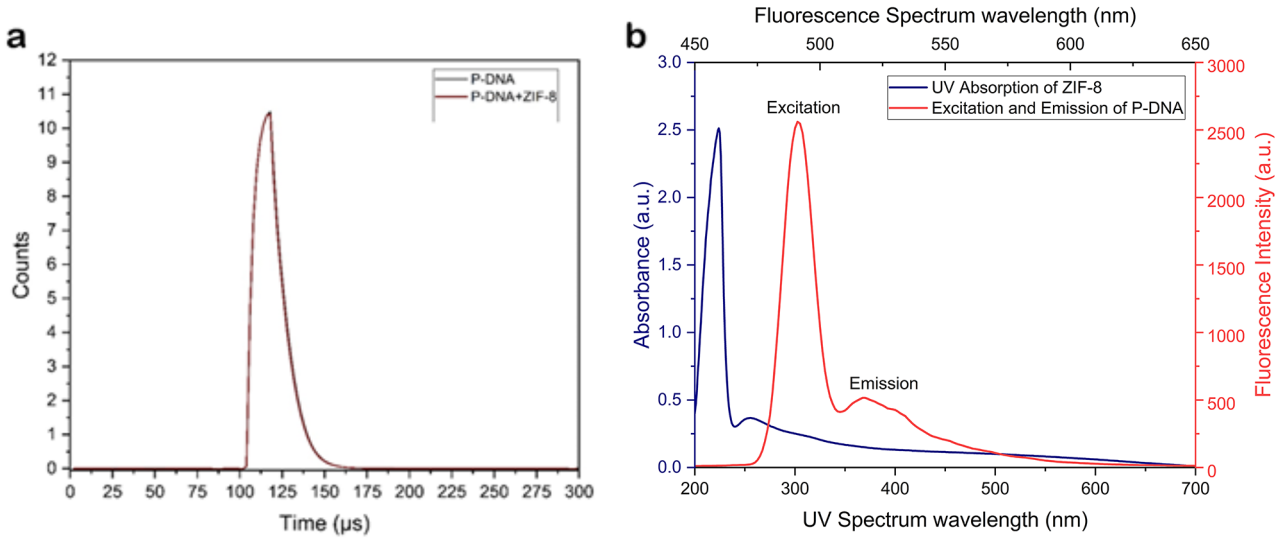


**Fig. 5**. (**a**) Fluorescence lifetime decay curve of P-DNA in the presence and absence of ZIF-8. (**b**) UV–Vis absorption spectrum of ZIF-8 and excitation and emission spectra of P-DNA.

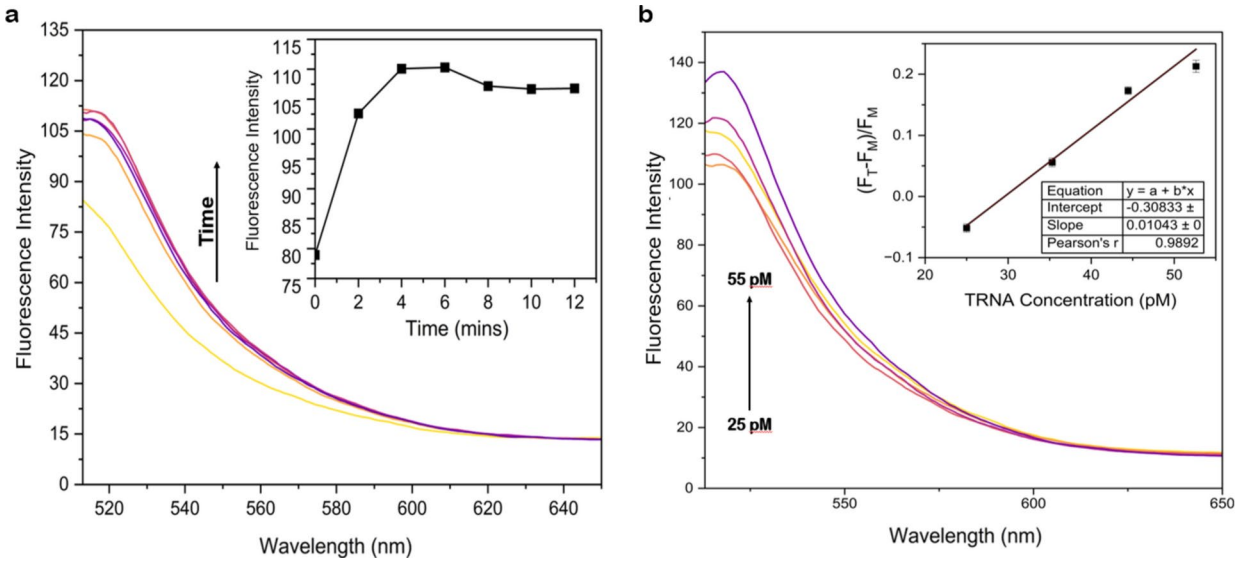


**Fig. 6**. (**a**) Fluorescence emission spectra of P-DNA with T-RNA for varying incubation time. (**b**) Fluorescence emission spectra of P-DNA with varying concentrations of T-RNA in TE buffer. Error bars represent the replicates standard deviation.

| MOF | Target Virus | $\%Q_e$ | Linear Range | LOD | References |
|---|---|---|---|---|---|
| ZIF-8 | COVID-19 RNA | 78.39 | 25–55 pM | 6.24 pM | This work |
| $\{[Zn(HCbdcp)_2]\cdot H_2O\}_n$ | HIV-1 ds-DNA | 73.0 | 1–80 nM | 10 pM | [42] |
| $\{[Dy(Cmdcp)(H_2O)_3](NO_3)\cdot 2H_2O\}_n$ | Ebola RNA | 60.0 | – | 120 pM | [46] |
| Al-MOF | HBV DNA | – | 100 aM-10 pM | 62.1 aM | [47] |
| Fe-MIL-88 | Zika RNA | – | 0.3 nM to 3 µM | 0.1 nM | [48] |
| $Cu(Dcbcp)(bpe)]_n$ | Dengue RNA | 92.0 | 1–60 nM | 332 pM | [45] |
| $Cu(Dcbcp)(bpe)]_n$ | Zika RNA | 92.0 | 0.5–70 nM | 192 pM | [45] |
| ZIF-8 | HIV-1 ss-DNA | 66.0 | 10–100 nM | 1.2 nM | [20] |

**Table 1**. Comparison between MOF-based platforms for virus biosensing.

*Sensitivity of the biosensor to target COVID-19 RNA*

In principle, adding the COVID-19 target RNA to the P-DNA@ZIF-8 system would create a hybrid RNA/DNA duplex with P-DNA. This hybrid duplex is stable and will detach the P-DNA from the MOF's surface, resulting in fluorescence recovery. Hence, the P-DNA@ZIF-8 complex could be deployed for biosensing of COVID-19 RNA sequences. This hypothesis was verified by measuring the fluorescence regenerated from exposure to COVID-19 T-RNA. Firstly, the optimum incubation time between P-DNA and T-RNA was obtained. As such, we plot in Fig. 6a the variations of the fluorescence intensity with the wavelength obtained at different incubation times. As shown in the inset plot of Fig. 6a, the fluorescence of P-DNA increases when the incubation time increases and saturates when it reaches 8 min at a concentration of 25 pM. Hence, 8 min was chosen as the operational condition for T-RNA detection.

Figure 6b shows the fluorescence regeneration upon adding T-RNA to the P-DNA@ZIF-8 complex. The results indicate that recovery of fluorescence dramatically depends on the T-RNA concentration. The fluorescence intensity showed a good linear correlation with the T-RNA concentration in the 25–55 pM range, with equation $(F_T-F_M)/F_M = 0.01043c_T - 0.00109$, $R^2 = 0.9892$. The detection limit was calculated using Eq. (3) to be as low as 6.24 pM. This low LOD implies that this biosensing platform has the potential to detect low-concentration COVID-19 T-RNA. Comparing the present results with those of MOFs reported in the literature for nucleic acids detection, as reported in Table 1, ZIF-8 shows relatively high quenching efficiency. Additionally, the present ZIF-8 biosensor has the least detection limit, indicating the high sensitivity of this biosensing platform. For instance, our biosensor exhibited superior sensing performance, in particular lower LOD, when compared to another ZIF-8-based sensor that was used for HIV detection[20]. One key factor that likely contributed to the enhanced sensitivity in our study is the synthesis method of ZIF-8. The solvothermal method has resulted in a more uniform particle size distribution and a larger surface area, as discussed earlier in Sect. "Detection of COVID-19 RNA sequence", improving the sensor performance. Furthermore, the better interactions between ZIF-8 and COVID-19 P-DNA also played a role in enhancing the rate of binding interactions, thereby reducing the response time of the biosensor. These differences highlight the importance of understanding and controlling

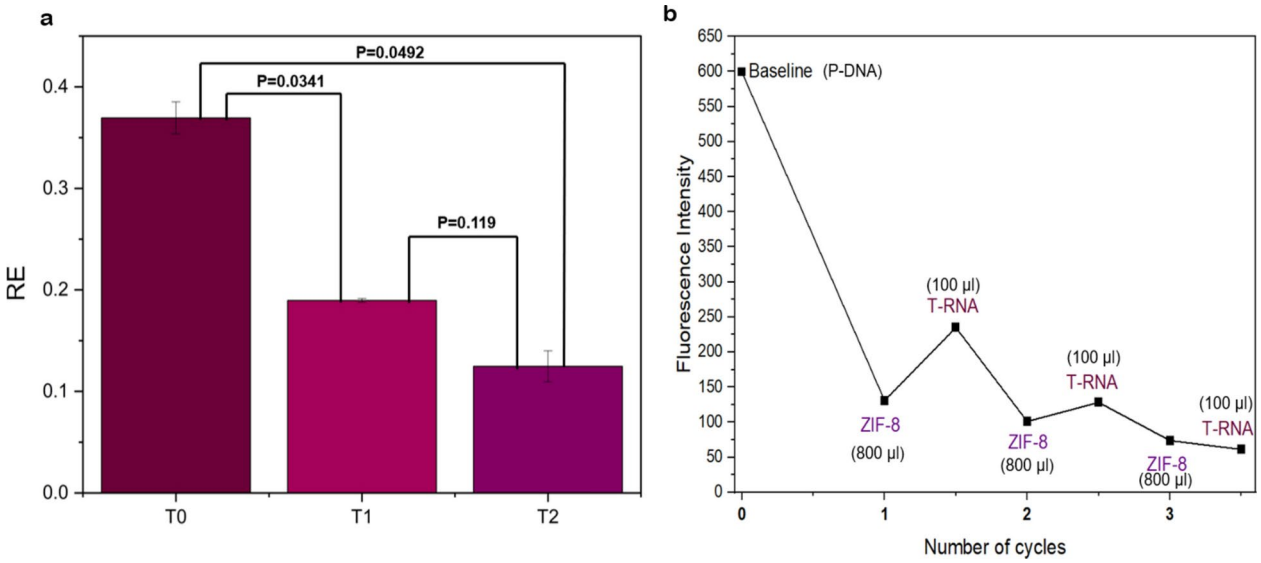


**Fig. 7**. (**a**) P-DNA@ZIF-8 system fluorescence recovery toward targets COVID-19 RNA T0, T1, and T2 at a fixed concentration. Error bars denote the STD of replicates, and p-values ($<0.05$) were calculated using the student's t-test two-pair analysis. (**b**) Recyclability of the ZIF-8 biosensor over three cycles. ZIF-8 and T-RNA solutions of 0.7 mg/ml and 200 pM were used respectively.

the synthesis of ZIF-8, and the batch-to-batch consistency, as small variations can impact the reproducibility and reliability of biosensors in real-world applications. However, the fluorescence intensity of probe DNA did not reach its original level upon adding enough T-RNA to the P-DNA@ZIF-8 system. This inadequate recovery could be because the MOF interacts with the hybrid DNA/RNA duplex[45]. The binding interactions of ZIF-8 with the P-DNA/T-RNA duplex can also be studied to verify this claim.

*Selectivity of the biosensor to RNA sequence*

To examine the selectivity of the P-DNA@ZIF-8 system, the P-DNA is hybridized with two different target RNAs. The target RNAs are one-base mismatched RNA T1 (5'-UACCGGCAGCAC**C**AGACAUCU-3′) and two-base mismatched RNA T2 (5'-UACCGGCAGCAC**C**AGAC**G**UCU-3'). As seen in Fig. 7a, when the same conditions were followed, the RE was found to be 0.19 for T1 and 0.14 for T2, and a much higher RE value of 0.42 was found for T0. It can be concluded that the fluorescence recovery of the biosensor is highly dependent on T0 than on T1 and T2. This experiment is repeated twice, and the standard deviation is calculated, as illustrated by the error bars in Fig. 7b. Moreover, statistical analysis was conducted for the target RNA sequences, and the p-values of T1 and T2 compared to T0 were found to be 0.0341 and 0.0492, respectively. The results indicate that the differences in T0, T1, and T2 results are statistically significant ($P<0.05$). Also, the p-value between T1 and T2 was calculated to be 0.119, implying no statistical difference in the results of T1 and T2. These results indicate that this sensing system is exceptionally selective for detecting COVID-19 RNA sequences in vitro.

Finally, a recyclability test was conducted to assess the reusability of the biosensor. Initially, the P-DNA was quenched by ZIF-8, and then the T-RNA was added to the P-DNA@ZIF-8 complex, resulting in observed fluorescence recovery. The same procedure was repeated for three cycles, and the results are shown in Fig. 7b. Remarkably, the fluorescence of P-DNA was successfully recovered over two cycles. Therefore, it is deduced that the P-DNA@ZIF-8 biosensor demonstrates a reliable performance over two consecutive cycles. We note that the biosensor is intended to be a low-cost and disposable kit for single use to secure high performance. Yet, the obtained results indicate its potential use several times.

## Conclusions

This paper investigates the feasibility of a ZIF-8-based biosensing platform for detecting COVID-19 RNA sequences. ZIF-8 was characterized through various tests, including XRD, FT-IR, TGA, BET, and FE-SEM. The results of the characterization tests were consistent with those reported in previously published studies. The experimental study confirmed the MOF's high crystallinity and thermal stability. The proposed biosensor exploits the fluorescence property of the ZIF-8 to detect COVID-19 RNA sequences. ZIF-8 attenuated the P-DNA fluorescence with $\%Q_e$ of 78.39%. The MOF can interact with the P-DNA by electrostatic and π-π stacking interactions, forming a P-DNA@ZIF-8 complex. It was further confirmed that FRET is less dominant than PET in the quenching mechanism. Running a HOMO–LUMO study can further confirm this claim. This biosensing platform showed high sensitivity towards COVID-19 RNA with very low LOD and incubation time of 6.24 pM, and 8 min, respectively. Furthermore, ZIF-8 showed high quenching efficiency and a much lower detection limit than other MOFs for sensing nucleic acids. Moreover, the ZIF-8-based biosensor was highly selective against one-base mismatched and two-base mismatched target RNA sequences. We also conducted a recyclability test which demonstrated the reliability of the P-DNA@ZIF-8 complex over two consecutive cycles,

indicating the high stability of the P-DNA@ZIF-8 complex over an extended period. The stability of the P-DNA@ZIF-8 complex over an extended period is a critical consideration for its practical applications, especially as a biosensor for detecting COVID-19 RNA sequences. A stable complex would ensure a reproducible, reliable, and accurate detection of COVID-19 RNA sequences, reducing the risk of false-positive or false-negative results. Also, the high stability of the P-DNA@ZIF-8 complex will provide a longer shelf life for the biosensor which is important when it comes to real-life applications. Moreover, this biosensor can be further modified to detect other viral RNA sequences, highlighting the potential versatility of the ZIF-8 platform. This potential arises from the tunable nature of ZIF-8, which allows it to detect a wide range of viral RNA sequences by using the corresponding P-DNAs, extending its application to other viruses beyond COVID-19. This applicability could make this ZIF-8 platform a powerful tool for multi-viral detection. These findings make the proposed ZIF-8-based biosensor a promising solution for rapid and sensitive COVID-19 diagnosis.

## Data availability

The datasets used and/or analysed during the current study available from the corresponding author on reasonable request.

Received: 3 May 2024; Accepted: 7 October 2024
Published online: 25 October 2024

## References

1. World Health Organization. WHO Coronavirus (COVID-19) Dashboard | WHO Coronavirus (COVID-19) Dashboard With Vaccination Data. https://covid19.who.int/ (2023).
2. Cheikh Ismail, L. et al. Impact of the coronavirus pandemic (COVID-19) lockdown on mental health and well-being in the United Arab Emirates. *Front. Psychiatry***12**, 265 (2021).
3. Bedford, J. et al. COVID-19: Towards controlling of a pandemic. *The Lancet***395**, 1015–1018 (2020).
4. Quraishi, M., Upadhyay, S. K. & Nigam, A. COVID-19 diagnostics: A panoramic view on its present scenario, challenges and solutions. *Proc. Natl. Acad. Sci. India Section B Biol. Sci.***92**, 709–721 (2022).
5. Tan, A. S. et al. The virological, immunological, and imaging approaches for COVID-19 diagnosis and research. *SLAS Technol.***25**, 522–544 (2020).
6. Carter, L. J. et al. Assay techniques and test development for COVID-19 diagnosis. *ACS Cent. Sci.***6**, 591–605 (2020).
7. Tahamtan, A. & Ardebili, A. Real-time RT-PCR in COVID-19 detection: Issues affecting the results. https://doi.org/10.1080/14737159.2020.1757437**20**, 453–454 (2020).
8. Orooji, Y. et al. An overview on SARS-CoV-2 (COVID-19) and other human coronaviruses and their detection capability via amplification assay, chemical sensing, biosensing, immunosensing, and clinical assays. *Nano-Micro Lett.***13**, 1–30 (2020).
9. Purohit, S., Rao, P. K. & Rawtani, D. Sampling and analytical techniques for COVID-19. in *COVID-19 in the Environment* 75–94 (Elsevier, 2022). https://doi.org/10.1016/B978-0-323-90272-4.00008-7.
10. Narwade, M., Shaikh, A., Gajbhiye, K. R., Kesharwani, P. & Gajbhiye, V. Advanced cancer targeting using aptamer functionalized nanocarriers for site-specific cargo delivery. *Biomater. Res.***27**, 42 (2023).
11. Sharabati, A. et al. Biomedical applications of metal–organic frameworks for disease diagnosis and drug delivery: A review. *Nanomaterials***12**, 277 (2022).
12. Gao, Y. et al. Two-dimensional porphyrin-Co9S8 nanocomposites with synergistic peroxidase-like catalysis: Synthesis and application toward colorimetric biosensing of H2O2 and glutathione. *Colloids Surf. A Physicochem. Eng. Asp.***568**, 248–258 (2019).
13. Wang, Y. et al. Metal-organic frameworks for virus detection. *Biosens. Bioelectron.***169**, 112604 (2020).
14. Abdel-Magied, A. F., Abdelhamid, H. N., Ashour, R. M., Zou, X. & Forsberg, K. Hierarchical porous zeolitic imidazolate frameworks nanoparticles for efficient adsorption of rare-earth elements. *Microporous Mesoporous Mater.***278**, 175–184 (2019).
15. Zhang, Q. et al. Fabrication of polyphenol-etched amino acid-modified ZIF-8 and their carbonic anhydrase-like catalytic activity. *Colloids Surf. A Physicochem. Eng. Asp.***682**, 132882 (2024).
16. Wang, Q., Sun, Y., Li, S., Zhang, P. & Yao, Q. Synthesis and modification of ZIF-8 and its application in drug delivery and tumor therapy. *RSC Adv.***10**, 37600–37620 (2020).
17. Park, K. S. et al. Exceptional chemical and thermal stability of zeolitic imidazolate frameworks. *Proc. Natl. Acad. Sci. U. S. A.***103**, 10186–10191 (2006).
18. Trino, L. D. et al. ZIF-8 metal-organic framework electrochemical biosensor for the detection of protein-protein interaction. *Chem. Mater.***33**, 1293–1306 (2021).
19. Abdelhamid, H. N. Zeolitic imidazolate frameworks (ZIF-8) for biomedical applications: A review. *Curr. Med. Chem.***28**, 7023–7075 (2021).
20. Pan, Y., Zhan, S. & Xia, F. Zeolitic imidazolate framework-based biosensor for detection of HIV-1 DNA. *Anal. Biochem.***546**, 5–9 (2018).
21. Li, J., Yang, K., Wu, Z., Li, X. & Duan, Q. Nitrogen-doped porous carbon-based fluorescence sensor for the detection of ZIKV RNA sequences: Fluorescence image analysis. *Talanta***205**, 120091 (2019).
22. Mehmandoust, M., Gumus, Z. P., Soylak, M. & Erk, N. Electrochemical immunosensor for rapid and highly sensitive detection of SARS-CoV-2 antigen in the nasal sample. *Talanta***240**, 123211 (2022).
23. Jiang, Z. W., Zhao, T. T., Li, C. M., Li, Y. F. & Huang, C. Z. 2D MOF-based photoelectrochemical aptasensor for SARS-CoV-2 spike glycoprotein detection. *ACS Appl. Mater. Interfaces***13**, 49754–49761 (2021).
24. Palanisamy, S. et al. One-step-one-pot hydrothermally derived metal-organic-framework-nanohybrids for integrated point-of-care diagnostics of SARS-CoV-2 viral antigen/pseudovirus utilizing electrochemical biosensor chip. *Sens. Actuators B Chem.***390**, 133960 (2023).
25. Zhao, X. et al. MIL-101(CuFe) Nanozymes with excellent peroxidase-like activity for simple, accurate, and visual naked-eye detection of SARS-CoV-2. *Anal. Chem.***95**, 1731–1738 (2023).
26. Rabiee, N. et al. Bioactive hybrid metal-organic framework (MOF)-based nanosensors for optical detection of recombinant SARS-CoV-2 spike antigen. *Sci. Total Environ.***825**, 153902 (2022).
27. Rabiee, N. et al. Porphyrin molecules decorated on metal–organic frameworks for multi-functional biomedical applications. *Biomolecules***11**, 1714 (2021).
28. Gumilar, G. et al. Rapid and label-free screening of SARS-CoV-2 virus in the infected human nasopharyngeal swab samples using UiO-66-modified SPR chip. *J. Ind. Eng. Chem.***127**, 467–475 (2023).
29. Reyes, S. et al. Metal organic framework encapsulated tamavidin-Gluc reporter: Application in COVID-19 spike antigen bioluminescent immunoassay. *Sens. Diagn.***1**, 1198–1208 (2022).

30. Alkhodairy, H., Naeem, M., Helal, A., Khalil, A. B. & Bajis, A. Development of Metal organic Framework Based Biosensor to Detect the Coronavirus (Covid-19). *bioRxiv* 2022.08.20.504642 (2022) https://doi.org/10.1101/2022.08.20.504642.
31. Rodrigues, M. G. F., Barbosa, T. L. A. & Rodrigues, D. P. A. Zinc imidazolate framework-8 nanoparticle application in oil removal from oil/water emulsion and reuse. *J. Nanopart. Res.***22**, 1–15 (2020).
32. Sharma, R. et al. Metal-organic framework ZIF-8 for exceptional HCl removal from Hydrogen gas by reaction. *Int. J. Hydrog. Energy***47**, 20556–20560 (2022).
33. Xie, Y. et al. Application of a novel Au@ZIF-8 composite in the detection of bisphenol a by surface-enhanced Raman spectroscopy. *Foods***12**, 813 (2023).
34. Nguyen, T. M. T. et al. A high-performance ZIF-8 membrane for gas separation applications: Synthesis and characterization. *Environ. Technol. Innov.***31**, 103169 (2023).
35. Kaur, H., Mohanta, G. C., Gupta, V., Kukkar, D. & Tyagi, S. Synthesis and characterization of ZIF-8 nanoparticles for controlled release of 6-mercaptopurine drug. *J. Drug Deliv. Sci. Technol.***41**, 106–112 (2017).
36. Bustamante, E. L., Fernández, J. L. & Zamaro, J. M. Influence of the solvent in the synthesis of zeolitic imidazolate framework-8 (ZIF-8) nanocrystals at room temperature. *J. Colloid Interface Sci.***424**, 37–43 (2014).
37. Nasrollahzadeh, M., Atarod, M., Sajjadi, M., Sajadi, S. M. & Issaabadi, Z. Plant-mediated green synthesis of nanostructures: Mechanisms, characterization, and applications. *Interface Sci. Technol.***28**, 199–322 (2019).
38. Fan, X. et al. Highly porous ZIF-8 nanocrystals prepared by a surfactant mediated method in aqueous solution with enhanced adsorption kinetics. *ACS Appl. Mater. Interfaces***6**, 14994–14999 (2014).
39. Taheri, M. et al. Stability of ZIF-8 nanopowders in bacterial culture media and its implication for antibacterial properties. *Chem. Eng. J.***413**, 127511 (2021).
40. Pinto, M. del C., Duque, A. L. & Macías, P. Fluorescence spectroscopic study on the interaction of resveratrol with lipoxygenase. *J. Mol. Struct.***980**, 143–148 (2010).
41. Cui, Y., Yue, Y., Qian, G. & Chen, B. Luminescent functional metal-organic frameworks. *Chem. Rev.***112**, 1126–1162 (2012).
42. Zhao, H. Q. et al. A zinc(II)-based two-dimensional MOF for sensitive and selective sensing of HIV-1 ds-DNA sequences. *Anal. Chim. Acta***922**, 55–63 (2016).
43. Yang, L., Liu, Y. L., Liu, C. G., Ye, F. & Fu, Y. A luminescent sensor based on a new Cd-MOF for nitro explosives and organophosphorus pesticides detection. *Inorg. Chem. Commun.***122**, 108272 (2020).
44. Asad, M. et al. Hydrazone connected stable luminescent covalent–organic polymer for ultrafast detection of nitro-explosives. *RSC Adv.***11**, 39270–39277 (2021).
45. Xie, B.-P. et al. Simultaneous detection of Dengue and Zika virus RNA sequences with a three-dimensional Cu-based zwitterionic metal–organic framework, comparison of single and synchronous fluorescence analysis. *Sens. Actuators B Chem.***254**, 1133–1140 (2018).
46. Qin, L. et al. A water-stable metal–organic framework of a zwitterionic carboxylate with dysprosium: A sensing platform for Ebolavirus RNA sequences. *Chem. Commun.***52**, 132–135 (2016).
47. Chen, G. et al. High-efficiency aluminum-metal organic framework/HEPES electrochemiluminescence system for ultrasensitive detection of HBV DNA. *Anal. Chem.***95**, 7030–7035 (2023).
48. Zhang, Y. W. et al. Metal-organic gel and metal-organic framework based switchable electrochemiluminescence RNA sensing platform for Zika virus. *Sens. Actuators B Chem.***321**, 128456 (2020).


## Acknowledgements

M. Ghommem is grateful to the Dana Gas Endowed Research Chair fund.

## Author contributions

Aya Elgazar: Investigation, Writing—original draft. Rana Sabouni: Supervision, Project Administration, Resources, Conceptualization, Review and Editing, Mehdi Ghommem: Supervision, Resources, Review and Editing. Amin F. Majdalawieh: Resources, Methodology, Review and Editing.

## Funding

We acknowledge the financial support of the American University of Sharjah via the faculty research grant (FRG22-C-E27). The work in this paper was supported by the Open Access Program (OAPCEN-1410-E00308) from the American University of Sharjah. This paper represents the opinions of the author(s) and does not mean to represent the position or opinions of the American University of Sharjah.

## Declarations

## Competing interests

The authors declare that they have no competing financial interests or personal relationships that could have appeared to influence the work reported in this paper.

## Additional information

**Correspondence** and requests for materials should be addressed to R.S.